The Astrophysical Journal, 789:44 (13pp), 2014 July 1 doi:10.1088/0004-637X/789/1/44


# THE ANGULAR CLUSTERING OF *WISE*-SELECTED ACTIVE GALACTIC NUCLEI: DIFFERENT HALOS FOR OBSCURED AND UNOBSCURED ACTIVE GALACTIC NUCLEI

E. Donoso[1,2], Lin Yan[3], D. Stern[4], and R. J. Assef[4,5,6]
[1] Instituto de Ciencias Astronómicas, de la Tierra, y del Espacio (ICATE), 5400 San Juan, Argentina
[2] Spitzer Science Center, California Institute of Technology, Pasadena, CA 91125, USA
[3] Infrared Processing and Analysis Center, Department of Astronomy, California Institute of Technology, Pasadena, CA 91125, USA
[4] Jet Propulsion Laboratory, California Institute of Technology, Pasadena, CA 91109, USA
[5] Núcleo de Astronomía de la Facultad de Ingeniería, Universidad Diego Portales, Av. Ejército 441 Santiago, Chile
*Received 2013 September 9; accepted 2014 April 15; published 2014 June 13*

## ABSTRACT

We calculate the angular correlation function for a sample of ∼170,000 active galactic nuclei (AGNs) extracted from the *Wide-field Infrared Survey Explorer* (*WISE*) catalog, selected to have red mid-IR colors ($W1-W2>0.8$) and 4.6 $\mu$m flux densities brighter than 0.14 mJy). The sample is expected to be >90% reliable at identifying AGNs and to have a mean redshift of $\langle z\rangle = 1.1$. In total, the angular clustering of *WISE* AGNs is roughly similar to that of optical AGNs. We cross-match these objects with the photometric Sloan Digital Sky Survey catalog and distinguish obscured sources with $r-W2>6$ from bluer, unobscured AGNs. Obscured sources present a higher clustering signal than unobscured sources. Since the host galaxy morphologies of obscured AGNs are not typical red sequence elliptical galaxies and show disks in many cases, it is unlikely that the increased clustering strength of the obscured population is driven by a host galaxy segregation bias. By using relatively complete redshift distributions from the COSMOS survey, we find that obscured sources at $\langle z\rangle \sim 0.9$ have a bias of $b = 2.9\pm0.6$ and are hosted in dark matter halos with a typical mass of $\log(M/M_{\odot}\,h^{-1}) \sim 13.5$. In contrast, unobscured AGNs at $\langle z\rangle \sim 1.1$ have a bias of $b = 1.6\pm0.6$ and inhabit halos of $\log(M/M_{\odot}\,h^{-1}) \sim 12.4$. These findings suggest that obscured AGNs inhabit denser environments than unobscured AGNs, and they are difficult to reconcile with the simplest AGN unification models, where obscuration is driven solely by orientation.

*Key words:* galaxies: active – infrared: galaxies – surveys

*Online-only material:* color figures

## 1. INTRODUCTION

In recent years, a large body of evidence suggests that the evolution and properties of active galactic nuclei (AGNs) are tightly linked not only to the properties of their hosting galaxies, but also to the environment that these host galaxies inhabit. The clearest example of this perhaps comes from radio-loud AGNs, which have long been known to be primarily hosted by giant, massive, elliptical galaxies, which are predominantly found in very dense environments (Matthews et al. 1964; Best et al. 2005; Donoso et al. 2010; Wylezalek et al. 2013). In general, X-ray AGNs have also been found to be strongly clustered (Gilli et al. 2005; Georgakakis et al. 2007; Coil et al. 2009), though X-ray AGNs out to $z\sim1$ with harder X-ray spectra, e.g., type-2, or obscured X-ray AGNs, are preferentially found in underdense regions (Tasse et al. 2011).

Large redshift surveys such as the Sloan Digital Sky Survey (SDSS; York et al. 2000) and the 2dF QSO Redshift survey (Croom et al. 2004) have enabled detailed studies of optical quasars and have shown that their clustering was larger in the past in such a way that optically selected quasars seem to be hosted by halos of roughly constant mass, a few times $10^{12}\,M_{\odot}$, out to $z\sim3$–4.

The advent of the *Spitzer Space Telescope* opened a new, mid-infrared (mid-IR) window to AGN populations, providing samples that are relatively insensitive to the dust extinction that affects quasar surveys in the optical, ultraviolet, and soft X-ray (<10 keV) bands. Stern et al. (2005) developed a simple selection technique based on IRAC colors that identifies luminous AGNs essentially independent of their obscuration, and thus it is particularly useful for identifying the dominant population of obscured AGNs that were largely missed in previous surveys (see also Lacy et al. 2004; Donley et al. 2012). However, it is the recent launch of the *Wide-field Infrared Survey Explorer* (*WISE*; Wright et al. 2010) that has made it possible to efficiently and robustly recover AGNs over the entire sky, including both unobscured and obscured sources.

The most widely accepted idea about the physical origin of obscuration is the presence of a thick dust torus that, when viewed sideways, blocks the central part of the AGN and hides many of the quasar-like features observed in unobscured AGNs (Antonucci 1993; Urry & Padovani 1995). The first indirect evidence in favor of a torus was the detection of polarized broad emission lines, characteristic of unobscured AGNs, in a fraction of well-known obscured AGNs due to the scattering toward the line of sight by free electrons just above (or below) the torus (see Heisler et al. 1997). As an alternative to orientation-driven or torus models of AGN obscuration, it is also plausible that at least part of obscuration could be caused by the interstellar medium of the host galaxy or by larger, ∼kiloparsec-scale clouds of cool dust (e.g., Martínez-Sansigre et al. 2009). Specifically, galaxy formation simulations by Hopkins et al. (2008) predict enhanced AGN activity after galaxy mergers, which is initially obscured by kiloparsec-scale dust clouds but is later laid bare as AGN feedback pushes out the obscuring material.

A basic prediction of the orientation-driven AGN unification models is that similarly selected AGNs should populate similar environments. While some differences are clearly evident based on intrinsic AGN luminosity or radio-loudness (e.g., Donoso et al. 2010; Falder et al. 2010), the expectation is that

[6] NASA Postdoctoral Program Fellow.

obscured (or type-2) and unobscured (or type-1) AGNs of similar luminosity and radio power should reside in similar environments. However, relatively little is known about the clustering of obscured AGNs, particularly those identified at mid-IR wavelengths. Gilli et al. (2009) studied the spatial clustering of X-ray AGNs at $z \sim 1$, finding no significant difference in clustering strength between obscured and unobscured X-ray-selected AGNs. Similarly, from a matched sample of powerful radio-loud AGNs at $1 < z < 3$, Wylezalek et al. (2013) found that radio-loud quasars (e.g., unobscured radio-loud AGNs) reside in similar environments to high-redshift radio galaxies (e.g., obscured radio-loud AGNs). In contrast, Hickox et al. (2011) analyzed a sample of 806 *Spitzer* mid-IR-selected quasars at $0.7 < z < 1.8$ in the Boötes field. They found marginal ($<2\sigma$) evidence that obscured quasars have a larger bias and populate more massive dark matter halos.

These studies, while powerful due to the availability of spectroscopic redshifts and/or a large number of photometric bands, suffer the typical limitations of deep pencil-beam surveys, providing samples of a few hundred objects at most. In this paper we adopt a complementary approach by combining the *WISE* and SDSS data sets over thousands of square degrees. We select AGNs based on the *WISE* 3.4 $\mu$m ($W1$) and 4.6 $\mu$m ($W2$) bands using selection criteria recently developed and demonstrated by Stern et al. (2012) and Assef et al. (2013). To quantify the clustering, we undertake a correlation analysis, which is arguably the most powerful method for studying the distribution of galaxies. The angular correlation function measures the projected clustering of galaxies by comparing the distribution of galaxy pairs relative to that of a random distribution. While a less direct probe than the spatial correlation function, $\xi(r)$, the angular correlation function is a powerful approach as it can be applied to wide-area surveys and large samples of galaxies, overcoming the limitations of small number statistics and cosmic variance. In this work we focus on the angular correlation of AGNs. Adopting a preliminary estimate of the redshift distribution of *WISE*-selected AGNs, we derive the absolute bias and estimate the typical mass of the dark matter halos that host them.

This paper is organized as follows. In Section 2 we describe the surveys used in this work. In Section 3 we describe mid-IR selection of AGNs using the *WISE* survey and detail the colors, morphologies, and redshift distribution of such sources. Section 4 presents the angular clustering measurements, Section 5 presents the results and conclusions, and Section 6 summarizes these results and discusses the implications of this work.

Throughout the paper we assume a flat concordance ΛCDM cosmology, with $\Omega_m = 0.3$, $\Omega_\Lambda = 0.7$, and $H_0 = 70\,\mathrm{km\,s^{-1}\,Mpc^{-1}}$. Unless otherwise noted, all magnitudes in this paper refer to the Vega system.

## 2. DATA

### 2.1. Wide-field Infrared Survey Explorer

The *WISE* satellite mapped the full sky in four bands centered at 3.4, 4.6, 12, and 22 $\mu$m (bands $W1$, $W2$, $W3$ and $W4$, respectively), achieving $5\sigma$ point-source sensitivities better than 0.08, 0.11, 1, and 6 mJy, respectively. Every part of the sky has been observed typically ∼10 times, except near the ecliptic poles, where the coverage is much higher. Astrometric precision is better than 0.″15 for high signal-to-noise ratio (S/N) sources (Jarrett et al. 2011), and the angular resolution is 6.″1, 6.″4, 6.″5, and 12″ for bands ranging from 3.4 to 22 $\mu$m.

This paper is based on data from the *WISE* All-sky Release, which comprises images and four-band photometry for over 563 million sources and has been publicly available since 2012 March. An object is included in this catalog if it (1) is detected with S/N > 5 in at least one of the four bands, (2) can be measured well in at least five frames, and (3) is not flagged as a spurious artifact in at least one band. We refer the reader to the *WISE* All-sky Release Explanatory Supplement for further details[7] (Cutri et al. 2011).

### 2.2. Sloan Digital Sky Survey Catalog

The SDSS (York et al. 2000; Stoughton et al. 2002) is a five-band photometric (*ugriz* bands) and spectroscopic survey that has mapped a quarter of the sky, providing photometry, spectra, and redshifts for about a million galaxies and quasars, and photometry for many more. The imaging reaches 50% completeness at $r = 22.6$ (Abazajian et al. 2009). The SDSS pipeline calculates several kinds of magnitudes. In this work we have adopted the model magnitudes (*modelMag*), which perform well for both bright and faint sources and provide unbiased galaxy colors. Magnitudes are corrected for Galactic reddening using the dust maps of Schlegel et al. (1998). When appropriate, SDSS magnitudes (nearly in the AB system) are converted into the Vega system using $m_{\mathrm{AB}} = m_{\mathrm{Vega}} + t$, where $t$ is estimated by projecting model stellar spectra into the SDSS $r$-band filter (for details, see `kcorrect`[8] software). In addition, SDSS asinh scale magnitudes are converted into Pogson logarithmic scale magnitudes (see the SDSS Web site for further details).

## 3. *WISE*-SELECTED AGNs

### 3.1. Mid-IR Selection

Mid-IR selection of AGNs relies on distinguishing the characteristic rising power-law AGN spectrum from the blackbody spectrum of stellar populations, which peak at rest frame 1.6 $\mu$m. This means that AGNs tend to be redder than normal galaxies in the mid-IR. This was initially shown in *Spitzer* data where simple IRAC-band color cuts isolate AGNs from other galaxy populations at $z \lesssim 3$ (e.g., Lacy et al. 2004; Stern et al. 2005). More recently, the *WISE* survey has proven very efficient in detecting AGNs using just the two shorter (and more sensitive) bands at 3.4 $\mu$m and 4.6 $\mu$m (Stern et al. 2012; Assef et al. 2013). Using empirical AGN and galaxy spectral templates, Assef et al. (2010) showed that even pure AGNs present typically red $W1 - W2$ colors out to $z \lesssim 3.5$ for reasonable values of dilution by the host galaxy light (e.g., see Figure 1 of Stern et al. 2012). Heavily extincted AGNs are of course even redder in $W1 - W2$. This contrasts with the bluer $W1 - W2$ colors of (1) Galactic stars, as only brown dwarfs with spectral types cooler than T5 have $W1 - W2 > 0.8$ (Kirkpatrick et al. 2011); and (2) normal galaxies out to $z \sim 1.2$. Thus, the primary contaminants to the red *WISE* color selections will be the coolest brown dwarfs, which are quite rare on the sky, and galaxies at $z \gtrsim 1.2$, which are effectively eliminated by our brightness cut, $W2 < 15.05$.

[7] *WISE* data products and documentation are available at http://irsa.ipac.caltech.edu/Missions/wise.html.
[8] Available at http://howdy.physics.nyu.edu/index.php/Kcorrect.

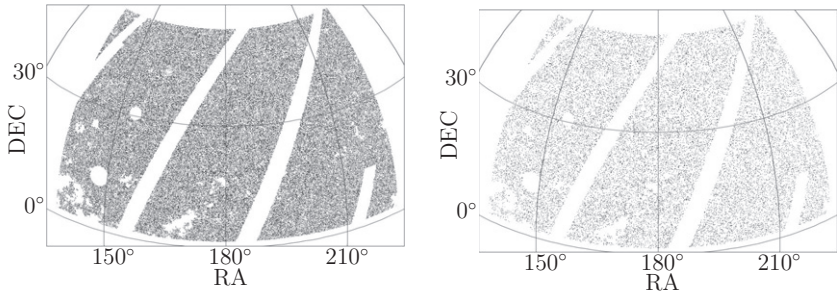


**Figure 1.** Equatorial coordinates of *WISE* AGNs projected onto the celestial sphere after the masking procedure described in Section 4.1 to remove areas with data of compromised quality (i.e., around Moon trails, large sources, bright stars, and areas of high Galactic absorption). The left panel shows all AGN candidates with $W1 - W2 > 0.8$ and $W2 < 15.05$, while the right panel shows *WISE* AGNs lacking optical counterparts in SDSS. No obvious large-scale differences are evident, suggesting that the latter are not related to Galactic sources, extinction, or image artifacts.

Using *WISE* data over the area covered by the COSMOS survey, Stern et al. (2012) demonstrated that a simple mid-IR color criterion is extremely robust at selecting AGN candidates. Selecting sources with $W1 - W2 > 0.8$ above the $10\sigma$ flux limit of 0.16 mJy at 4.6 $\mu$m ($W2 < 15.05$, Vega) identifies a large population of AGNs that is ∼95% reliable and nearly 80% complete with respect to the *Spitzer* AGN selection of Stern et al. (2005). These criteria identify 62 AGNs per deg$^2$, as compared to the ∼20 quasars per deg$^2$ identified by the optical SDSS quasar selection algorithm, which is sensitive to AGNs of similar intrinsic luminosity (Richards et al. 2002). We construct our AGN sample by applying the same selection criteria over a much larger area covered by SDSS. In our sample, we only allow sources whose $W1$ and $W2$ photometry is unaffected by diffraction spikes, scattered light, persistence, or optical ghosts (*ccflag* $= 0$ in both $W1$ and $W2$). Assef et al. (2013) reports on *WISE* selection of AGNs down to $W2 < 17.1$ in the higher ecliptic latitude and thus deeper Boötes field. We refer the reader to their work for a useful comparison of *WISE* AGN selection at various depths. We note that, ignoring $W1 - W2$ color for the moment, typical $L^*$ galaxies can be observed by *WISE* up to $z \sim 1.2$ at a $5\sigma$ sensitivity ($W2 = 15.85$; see Figure 6 of Yan et al. 2013). With our conservative flux density cut, $W2 = 15.05$, only the brightest, several $L^*$ galaxies will be detected by *WISE* at $z \gtrsim 1$.

Using the selection criteria of $W1 - W2 > 0.8$ and $W2 < 15.05$, we selected 176,467 *WISE* AGN candidates over an effective area of 3363 deg$^2$ (see Section 4.1 for details about the angular mask). The $W2 < 15.05$ mag cut guarantees that 99.7% of candidates are detected with $S/N_{W2} > 10$ and that 99.98% have $S/N_{W2} > 9$, while the mean $S/N_{W2}$ of the sample is ∼20.

The 176,467 selected AGN candidates are cross-matched with the SDSS photometric catalog. Using a matching radius of 1.″5, we find 152,672 (86.5%) *WISE* AGN candidates with single optical matches, 6095 (3.5%) sources with two or more SDSS counterparts, and 17,700 (10.0%) *WISE* AGN candidates without an optical source listed in the SDSS database. The multiple optical matches are mostly due to spurious detections of large sources split into multiple components or, in a few cases, real interacting galaxy systems. These *WISE* unresolved close galaxy pairs are on scales $\theta < 0.^\circ001$, well below the spatial scales relevant in this work. The clustering analysis of galaxies on such small angular scales is beyond the scope of this paper, as it would require full knowledge of the deblending performance of the SDSS and *WISE* pipelines. Therefore, we focus here on *WISE* AGN candidates with single or no optical counterparts. Note that so far we have not applied any constraints on SDSS magnitudes, so that among the 152,672 single *WISE*–SDSS matches, about 5% are fainter than the $r = 22.6$ 50% completeness limiting magnitude of SDSS but are nevertheless listed in the SDSS catalog. To ensure that the *WISE* AGNs without SDSS counterparts are all real sources and not artifacts, we have visually inspected the *WISE* and SDSS images of 1000 randomly selected objects. We did not find any artifacts from the inspection. In addition, Figure 1 shows the equatorial coordinates of all *WISE* AGNs considered in this study, as well as the *WISE* AGNs lacking optical counterparts in the SDSS database. In the latter case, we have closely inspected their spatial distribution projected on the sky. There are no obvious large-scale patterns, suggesting that the lack of an optical identification is intrinsic to the sources, and not related to image artifacts, Galactic objects, or large-scale extinction.

Finally, to further demonstrate that the *WISE* AGN selection is robustly identifying AGNs, we investigate the fraction of *WISE*-selected AGNs with X-ray counterparts in the 60 ks exposures of the *XMM-Newton* wide-field (∼2 deg$^2$) survey of the COSMOS field (XMM-COSMOS; Hasinger et al. 2007; Brusa et al. 2010). We find that ∼75% of *WISE*-selected AGNs are X-ray detected, with the remaining ∼25% expected to be fainter and/or heavily obscured AGNs missed by the *XMM-Newton* observations. Indeed, deeper *Chandra* observations of the central half of the COSMOS field (Elvis et al. 2009) detect 87% of the *WISE*-selected AGNs. Similar results were found previously in Stern et al. (2012), though that work imposed an $S/N_{W2} > 10$ cut, as opposed to the flux density cut used here.

### 3.2. Red and Blue AGNs in WISE

As mid-IR observations are relatively insensitive to obscuration by dust and optical observations are significantly affected by dust extinction, type-2 or obscured AGNs can be isolated by comparing *WISE* and SDSS fluxes (Stern et al. 2012; Yan et al. 2013). Hickox et al. (2007, 2011) applied a similar method in the Boötes field using IRAC 4.5 $\mu$m and *R*-band photometry to differentiate obscured and unobscured AGNs. For the sake of completeness, we note, however, that there is no rigorous and unique definition to differentiate obscured and unobscured AGNs across all wavelengths.

In this work, we divide the *WISE* AGN sample according to $r - W2$ color. Figure 2 illustrates that AGNs show a bimodal color distribution that separates two populations of AGNs. Those with colors redder than $r - W2 = 6$ are, of course, optically faint (or undetected in SDSS), but nevertheless well detected at 4.6 $\mu$m. We call these "red AGNs," in contrast with

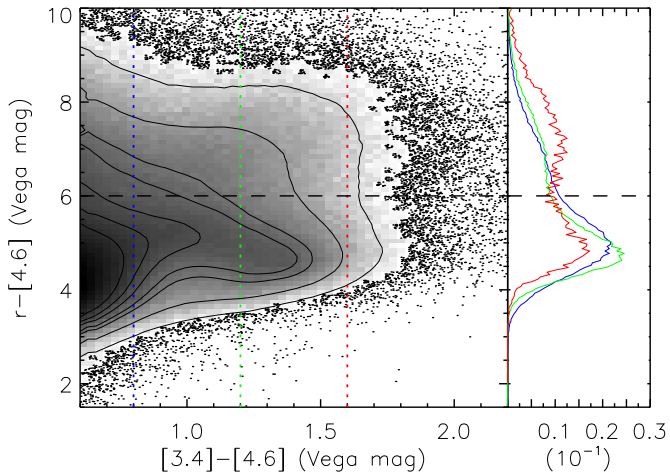


**Figure 2.** *WISE*-selected AGNs split into red (e.g., obscured) sources with $r-W2 > 6$ and unobscured AGNs with $r-W2 \leqslant 6$. The gray-scale, contoured region corresponds to high-density regions, while individual points are shown in areas of low density. Histograms in the right panel illustrate the marked bimodality of the distribution at increasingly redder colors, indicated by the vertical dotted lines in the left panel.

(A color version of this figure is available in the online journal.)

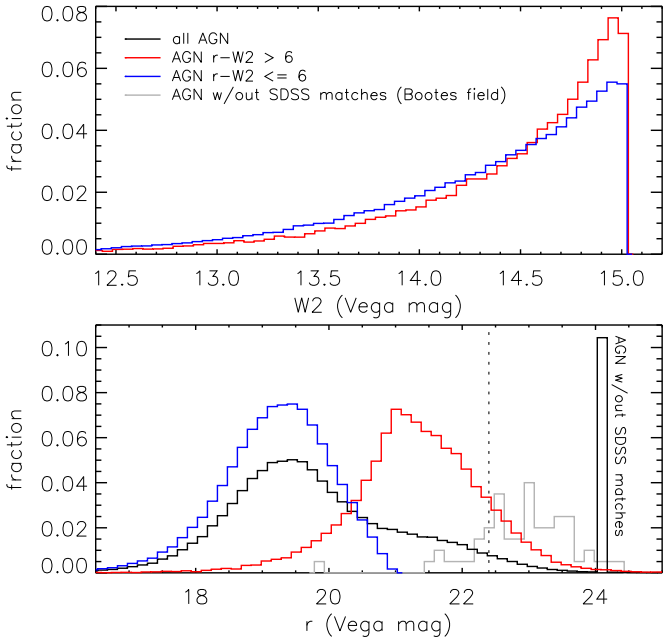


**Figure 3.** Top: $W2$ magnitude distribution of *WISE* AGN candidates split into obscured ($r - W2 > 6$, red line) and unobscured AGNs ($r - W2 \leqslant 6$, blue line). The former sources are slightly fainter on average, but both distributions are very similar. Bottom: optical $r$-band magnitude distribution of *WISE* AGN candidates showing the effect of the $r - W2$ color cut. For ease of plotting, the single bin at $r = 24$ represents AGNs that lack an optical match in SDSS; recall that the 50% completeness limit of SDSS is at $r = 22.6$ (Vega, Pogson scale; vertical dashed line). We show the $R$-band magnitudes for 61 such AGNs that are in the deeper Boötes field (gray line); most, in fact, turn out to be brighter than $r \sim 24$.

(A color version of this figure is available in the online journal.)

"blue AGNs" that are relatively bright at both mid-IR and optical wavelengths. We fold AGNs lacking optical matches into the red AGN sample. As shown in Hickox et al. (2007), the red population is more closely associated with type-2 AGNs, while the blue population is associated with type-1 AGNs, e.g., AGNs presenting broad emission lines in optical spectroscopy. In total, about 60,000 sources are selected as red AGN candidates, implying a type-1 fraction of roughly 55%, similar to the fraction found by Assef et al. (2013) for luminous AGNs with bolometric luminosities exceeding a few times $10^{46}$ erg s$^{-1}$. In Section 3.4 we evaluate the model selection function of red and blue AGNs to test the reliability of the $r - W2$ criteria to separate type-1 and type-2 AGNs.

Figure 3 (top panel) shows the $W2$ magnitude distribution of red and blue *WISE*-selected AGNs. Although red AGNs seem slightly fainter at mid-IR wavelengths in general, both subsamples have similar distributions, suggesting that there is no strong bias due to the $r - W2$ color cut. The bottom panel shows the distribution of SDSS $r$-band magnitudes (corrected for Galactic reddening, converted to Vega and in the Pogson scale). Blue AGNs are considerably brighter, peaking at $r \sim 19.3$ and falling steeply at $r \gtrsim 19.5$. Most red AGNs are fainter, peaking around $r \sim 21.2$ and extending to fainter magnitudes, beyond the nominal SDSS completeness limit. A considerable fraction (10%) of *WISE* AGN candidates are simply undetected by SDSS; we indicate such sources with a single bin at $r = 24$. The Boötes field has considerably deeper $R$-band photometry available, reaching $R \sim 26$ ($5\sigma$, point source; Jannuzi et al. 2010). There are 61 SDSS-undetected, *WISE*-selected AGNs in Boötes. Their $R$-band magnitude distribution peaks at $R \sim 23$ (gray line), with all sources having optical counterparts. This again illustrates the optical faintness but detectability of essentially all *WISE*-selected AGNs. Finally, we note that the fraction of *WISE*-selected AGNs with X-ray counterparts in the *XMM-Newton* wide field at the 0.5−10 keV band is ∼83% for blue AGNs ($r - W2 \leqslant 6$), dropping to ∼68% for red AGNs ($r - W2 > 6$). These high detection rates further demonstrate the reliability of our sample.

### 3.3. Morphologies

Figure 4 shows the range of optical morphologies of *WISE*-selected AGNs. For three candidates in the COSMOS field, we display ∼1′-on-a-side images in *WISE* $W2$ and SDSS $r$ band and ∼10″-on-a-side *Hubble Space Telescope* (*HST*) images in the $F814W$ filter. The top row shows an example of a blue, or unobscured, *WISE*-selected AGN: WISE J100025.25+015852.1 is an optically bright, optically unresolved SDSS quasar ($r - W2 = 4.6$) at redshift $z = 0.372$. The middle row shows an example of an optically faint, or red, obscured *WISE*-selected AGN: WISE J100005.98+015453.1 is an optically faint source detected by SDSS ($r - W2 = 6.7$). Trump et al. (2007) report a redshift of $z = 0.969$ for this X-ray-detected, optically resolved source and classify it as type-2 AGN based on its spectrum. The bottom row shows an example of the 10% of *WISE*-selected AGNs that are undetected by SDSS: WISE J100153.32+021928.3 is undetected by SDSS ($r - W2 \geqslant 7.5$) but is detected by both *HST* and *XMM-Newton*. The source has a photometric redshift of $z = 1.512$.

Optical morphologies offer an additional observable with which to investigate the *WISE* AGN selection. Luminous, unobscured, or type-1 AGNs are typically unresolved at optical wavelengths, which was one of their foundational attributes that led to the name "quasar," or quasi-stellar radio source. We have known for several decades now that only ∼15% of quasars are radio-loud, with little variation in this fraction with either redshift or optical luminosity, at least at the high-luminosity end (e.g., Stern et al. 2000). Similarly, mid-IR selection is showing that unresolved, unobscured quasars represent a minority population of luminous AGNs. Indeed, using the SDSS `type` flag

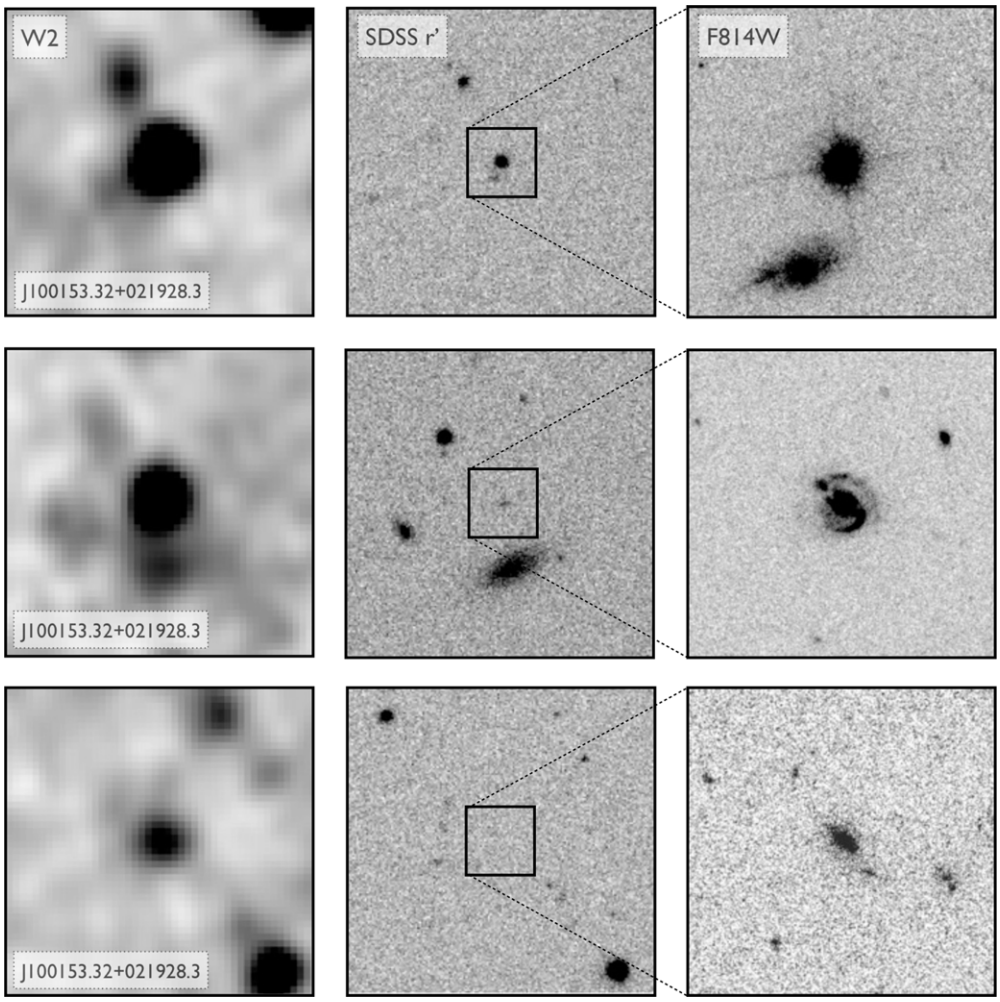


**Figure 4.** Images of three *WISE*-selected AGNs in the COSMOS field, showing the range of optical morphologies. From left to right, the columns show *WISE* $W2$ ($\sim 1'$ on a side), SDSS $r$ ($\sim 1'$ on a side), and *HST* F814W ($I_{814}$; $\sim 10''$ on a side). North is up, and east is to the left. The top row shows an example of a blue or unobscured *WISE*-selected AGN at $z = 0.372$. The middle row shows an example of an optically faint, red, or obscured *WISE*-selected AGN at $z = 0.969$; this source is X-ray detected and classified as a type-2 AGN (Trump et al. 2007). The bottom row shows an example of the 10% of *WISE*-selected AGNs that are undetected by SDSS. This source is detected by *XMM-Newton* and has a photometric redshift of $z = 1.512$. See text for further details on the individual sources.

to discriminate morphologies, we find that only ∼55% of the *WISE*-selected AGNs considered in this paper are classified as unresolved point sources.

We use the COSMOS field to characterize how morphology depends on optical-to-mid-IR color for *WISE*-selected AGNs. Figure 5 shows a histogram of the optical-to-mid-IR colors of the 82 *WISE*-selected AGNs with *HST* Advanced Camera for Surveys (ACS) (F814W) imaging in COSMOS to our $W2 = 15.05$ depth, coded by optical morphology. Fifteen of the sources are undetected by SDSS in the $r$ band and are simply plotted at $r - W2 = 10$; all 15 of these sources are detected in the deeper *HST* $F814W$ imaging and are spatially resolved. Indeed, of the 28 red AGN candidates with $r - W2 > 6$, only 1 (4%) is unresolved. This supports our expectation that red optical-to-mid-IR colors select a clean sample of obscured AGNs with little contamination from unobscured AGNs.

Of the 54 blue AGN candidates, 35 (65%) are unresolved. Figure 6 shows the $r - W2$ color versus redshift for these blue AGN candidates, with symbols indicating their *HST* morphologies. As we will show in the next section, most of the resolved AGNs—e.g., likely obscured AGNs contaminating our blue AGN selection—are at lower redshift ($z < 0.5$) and, in fact, reside in the redder end of our blue AGN selection. However, Figure 5 also clearly shows that it is not feasible to simply make a bluer $r - W2$ cut to separate obscured (e.g., resolved) and unobscured (e.g., unresolved) AGNs.

To characterize the host galaxies of *WISE*-selected candidates, we performed more detailed visual classifications on the *HST* ACS image cutouts (independently by three of the four authors; as we agreed for the majority of objects, we report the average here). For red AGNs, we find that 54% (15) are disk galaxies or interacting systems, 32% (9) are elliptical or point sources, and the remaining 14% (4) have uncertain morphology. This contrasts with blue AGNs, where we find that 20% (11) are disk galaxies and 80% (43) are either point sources (most) or ellipticals. These results are consistent with the work of Griffith & Stern (2010), who studied the morphology of AGNs in COSMOS selected at radio, X-ray, and mid-IR wavelengths. That work found that the red mid-IR-selected AGNs consist of 63% disk galaxies, 22% point sources/ellipticals, and 15% other morphology, while the blue AGNs consist of 15% disk galaxies and 85% point sources/ellipticals. The main conclusion we wish to draw here is that given its high fraction of disk galaxies, the red AGN sample is not dominated by typical red sequence galaxies. In fact, the red AGNs have a higher fraction of disk galaxies than the blue AGNs.

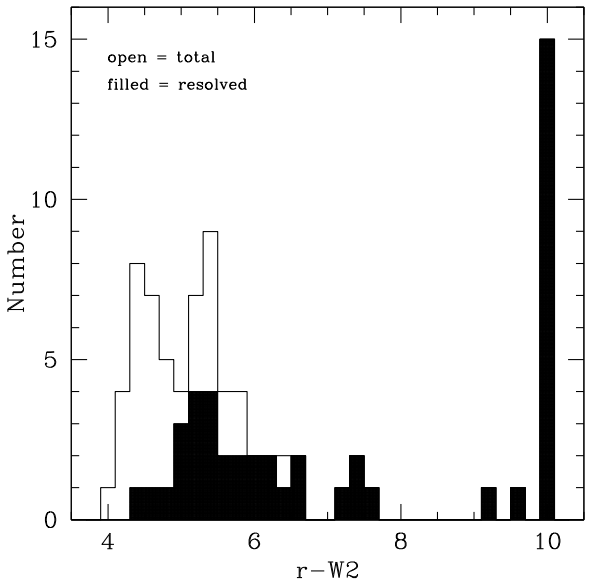


**Figure 5.** Histogram of number of *WISE*-selected AGN in the *HST*-imaged section of the COSMOS field to our $W2 = 15.05$ depth as a function of $r - W2$ color. The total (open + filled) histogram shows the total number of sources, while the filled histogram shows the subset that are spatially resolved by *HST*. Sources that are undetected by SDSS in the $r$ band are plotted at $r - W2 = 10$.

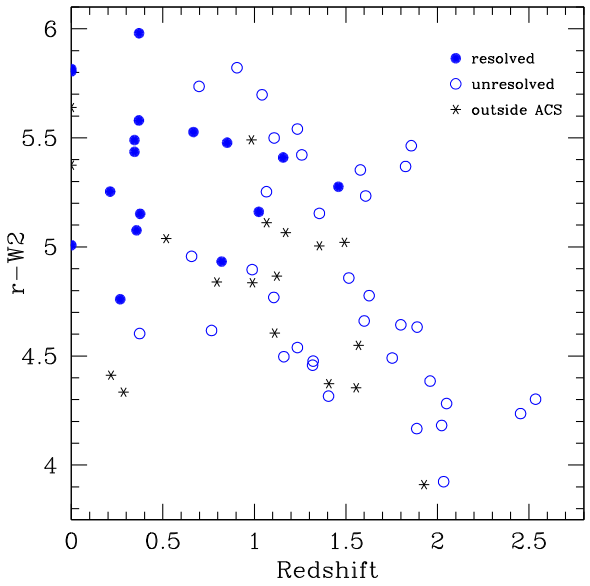


**Figure 6.** $r - W2$ color vs. redshift for blue AGN candidates in the COSMOS field that have *HST* $I_{814}$ morphologies available. Spatially resolved sources are indicated by filled blue symbols, while unresolved sources are marked with open symbols. A large fraction of AGNs at low redshift ($z < 0.5$) are clearly resolved and still meet the blue AGN selection criteria, suggesting that our low-redshift, blue AGN sample is likely a mixture of obscured/unobscured AGN populations.

(A color version of this figure is available in the online journal.)

As further discussed in Section 5.3, this suggests that it is unlikely that a bias in host galaxy type (favoring red AGNs in early-type hosts and blue AGNs in late-type hosts) could have a large impact in the interpretation of the clustering results presented in Section 5.

### *3.4. Redshift Distribution and Selection Function*

Given the difference in optical flux introduced by the $r - W2$ cut, it is not unreasonable to expect differences in the redshift distribution of blue and red AGNs. In order to understand the

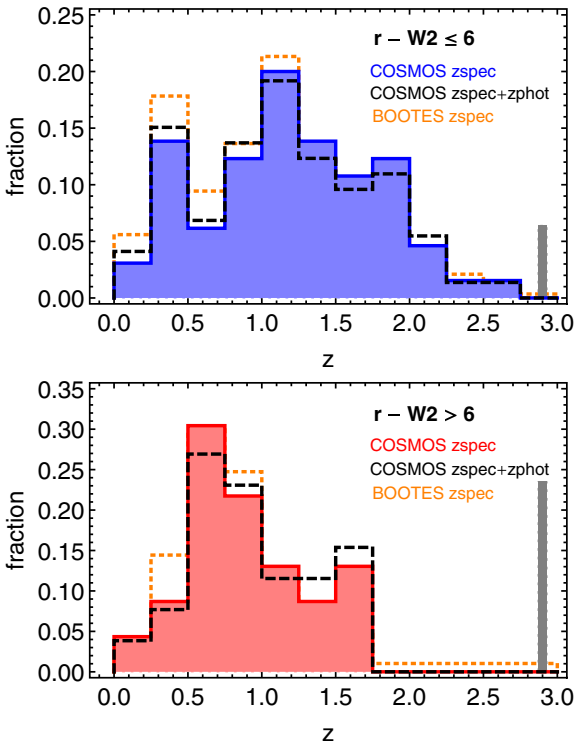


**Figure 7.** Redshift distribution of *WISE*-selected AGNs in COSMOS. The top panel highlights the blue AGNs ($r - W2 \leqslant 6$), with the solid histogram showing sources with spectroscopic redshifts and the dashed histogram including five additional photometric redshifts. The five sources lacking both spectroscopic and photometric redshifts are plotted at $z = 2.9$ (gray bar). The bottom panel highlights the red AGNs, again distinguishing spectroscopic redshifts (solid histogram) and photometric redshifts (dashed). The eight sources lacking both spectroscopic and photometric redshifts are plotted at $z = 2.9$ (gray bar). For reference, we also show in both panels the corresponding redshift distributions in Boötes (dotted orange).

(A color version of this figure is available in the online journal.)

redshift distribution and properties of *WISE* AGN candidates, we have matched our list to publicly available spectroscopy in the COSMOS field and recent spectroscopic observations (see Stern et al. 2012 for details about the compiled list of spectroscopic and photometric redshifts).

Figure 7 shows the redshift distribution of the 112 *WISE*-selected AGNs available in COSMOS, of which 88 have spectroscopic redshifts and 11 have photometric redshifts (plus 13 objects with no redshift information available). The top panel highlights the blue AGNs ($r - W2 \leqslant 6$), including five sources, plotted at $z = 2.9$, that lack both spectroscopic and photometric redshifts. The distribution peaks around $z \sim 1.1$ and extends up to $z \sim 2.5$, with most of the sources at $0.8 < z < 2$. There is an indication of a second smaller peak at $z \sim 0.5$, most probably (as we will see later) due to type-2 AGNs that enter into the redder part of our blue sample selection at low redshift. For reference, we also show the spectroscopic redshifts of 536 *WISE* AGN candidates within the Boötes field (dashed histogram), obtained from the AGN and Galaxy Evolution Survey (AGES; Kochanek et al. 2012). This survey has different completeness levels for different galaxy samples ($I < 20$ for galaxies, $I < 22.5$ for AGNs, but with varying priority levels based on their brightness at mid-IR, 24$\mu$m, radio, and X-ray energies) and therefore a complicated redshift selection function. However, considering the differences in target selection as compared to COSMOS (which essentially targeted every source to $R \sim 25$), the two

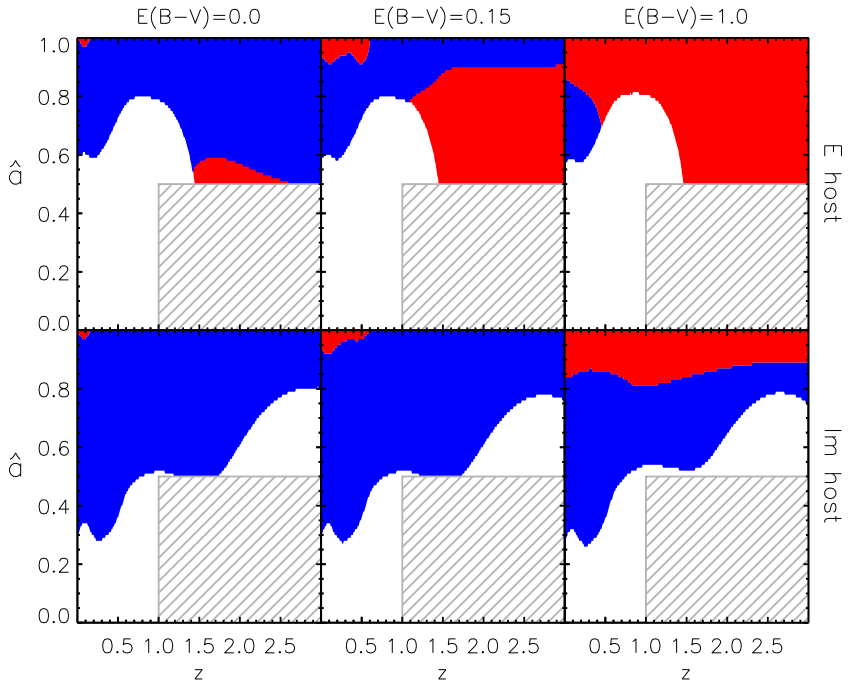


**Figure 8.** Model selection function of blue and red AGNs constructed using mock objects that adopt the AGN and galaxy SED templates of Assef et al. (2010). The parameter $\hat{a}$ is the fraction of the bolometric luminosity coming from the AGN component (see the text for details). Each panel shows, for a given host galaxy type (E or Im) and reddening value, whether an object would be targeted as a blue AGN (blue region), a red AGN (red region), or an inactive galaxy (white region). The gray hatched area marks the region where *WISE* is not sensitive due to its shallowness given our $W2 < 15.05$ brightness cut, namely, $z > 1$ host-galaxy-dominated objects. While essentially all of the unobscured AGNs (left panels) are correctly identified as blue AGNs, some fraction of obscured AGNs (right panels) will have blue AGN colors. Phrased differently, we expect the red AGN sample to be a relatively pure sample of obscured AGNs, while the blue AGN sample will primarily be unobscured AGNs, but will have some contamination from obscured sources.

(A color version of this figure is available in the online journal.)

distributions agree remarkably well. This suggests that both are not far from the true redshift distribution of *WISE*-selected AGNs with blue $r - W2$ colors. The bottom panel in Figure 7 shows the corresponding distributions for *WISE*-selected AGNs with red $r - W2$ colors, including eight sources lacking both spectroscopic and photometric redshifts plotted at $z = 2.9$. Red AGN candidates peak at lower redshift, around $z \sim 0.8$, and extend up to $z \sim 1.8$. Again, the agreement with AGES redshifts in the Boötes field is notable.

To further understand the nature of the differences in redshift among the red and blue AGN samples, we model their selection function by constructing mock objects using the AGN and galaxy spectral energy distribution (SED) templates from Assef et al. (2010). The parameter $\hat{a} \equiv L_{\rm AGN}/(L_{\rm host}+L_{\rm AGN})$ quantifies the fraction of the bolometric luminosity coming from the AGN component (see Assef et al. 2010, 2013 for details). Figure 8 shows whether an object with a given host galaxy type (E or Im), $\hat{a}$ value, and reddening toward the accretion disk, parameterized by $E(B-V)$, would be targeted as a blue AGN ($r - W2 \leqslant 6$, blue region), as a red AGN ($r - W2 > 6$, red region), or as an inactive galaxy ($W1 - W2 < 0.8$, white region). As expected, at low $\hat{a}$, most systems are characterized as normal galaxies. The panels at $E(B-V) = 0.0$ and $E(B-V) = 1.0$ highlight the extreme cases of a zero reddening or a heavily extincted AGN; the typical boundary between type-1 and type-2 AGNs corresponds to a reddening of $E(B-V) = 0.15$ (see Assef et al. 2013 for details). The gray hatched area marks the region where *WISE* is not sensitive due to the shallowness imposed by our $W2 < 15.05$ flux density requirement, namely, $z \gtrsim 1$ host-galaxy-dominated objects. This figure shows that while it is very unlikely to misclassify a blue AGN as a red one, the opposite happens for a significant fraction of parameter space, suggesting that our red AGN selection constitutes a reliable yet incomplete type-2 AGN sample, while our blue sample consists of a mixture of type-1 and type-2 AGNs.

We also used the deep, multi-wavelength data available in the Boötes field to do detailed SED modeling of *WISE*-selected AGNs and explore how reddening relates to $r - W2$ color for blue and red AGN candidates as a function of redshift. This is shown in Figure 9. The reddening parameter $E(B-V)$ is derived by fitting the AGN and galaxy SED templates of Assef et al. (2010). As expected, red AGNs tend to show considerable reddening at all redshifts, with $E(B-V) \gtrsim 0.7$, while blue AGNs are mostly unreddened above $z \sim 0.5$. However, below this redshift, blue AGNs can sometimes show large reddening values, consistent with the idea that some of these objects might well be type-2 AGN interlopers in the blue sample. As shown in the bottom panel of Figure 9, the distributions of $\hat{a}$ are strongly peaked toward high values, with most red AGNs above $\hat{a} \sim 0.8$, and a minor fraction of blue AGNs with $0.6 < \hat{a} < 0.8$. This means that while the blue area in the bottom right panel of Figure 8 is large, only a minority of sources could be potentially biased due to the galaxy host type (i.e., selected as blue AGNs due to the presence of an Im galaxy host).

## 4. ANGULAR CORRELATION ANALYSIS

### 4.1. The Angular Correlation Function

A standard tool to measure galaxy clustering is the two-point angular correlation function, $w(\theta)$. It is defined as the probability that a given pair of galaxies separated by an angle $\theta$ on the sky

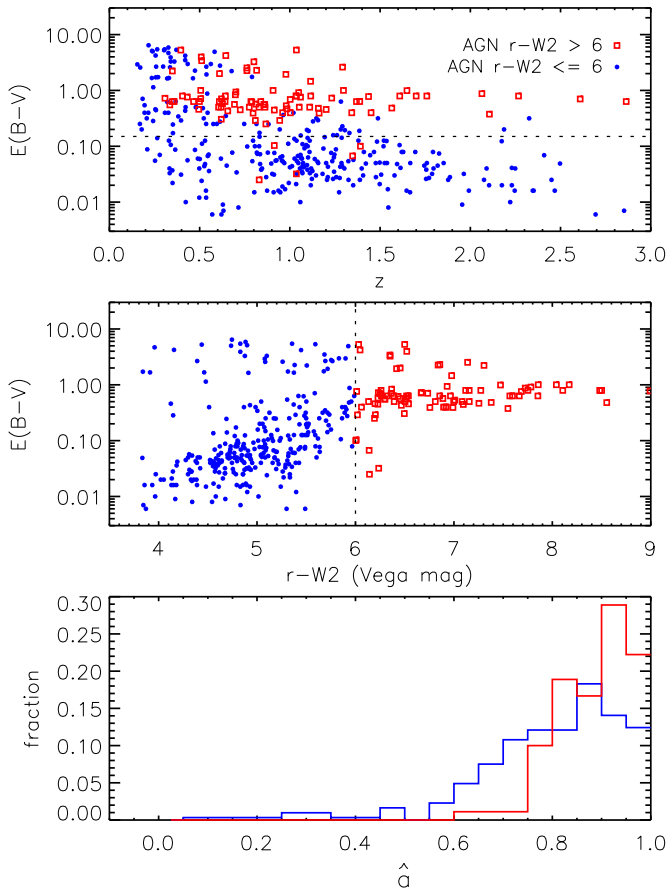


**Figure 9.** Dependence of the reddening parameter, $E(B-V)$, on redshift (top panel) and $r-W2$ color (middle panel) for blue (filled symbols) and red (open squares) *WISE*-selected AGN candidates in the Boötes field. $E(B-V)$ is derived by fitting the AGN and galaxy SED templates of Assef et al. (2010). In general, red AGNs tend to have considerable reddening at all redshifts, while blue AGNs are mostly unreddened at $z > 0.5$ but can have large reddening values at lower redshift. The fiducial type-1/type-2 separation is around $E(B-V) = 0.15$. The bottom panel shows the distribution of the $\hat{a}$ parameter (see Section 3.4 for definition) for red and blue AGNs.

(A color version of this figure is available in the online journal.)

are contained within a solid angle $d\omega$

$$dP = n(1 + w(\theta))d\omega, \quad (1)$$

where $n$ is the mean number density of galaxies. In practice, $w(\theta)$ is calculated by counting pairs of galaxies in annuli of different radii and comparing with the corresponding counts in a random sample of galaxies. To estimate $w(\theta)$, we use the Landy & Szalay (1993) estimator, given by

$$w(\theta) = \frac{\mathrm{DD} - 2\mathrm{DR} + \mathrm{RR}}{\mathrm{RR}}, \quad (2)$$

where DD, DR, and RR are the normalized data–data, data–random, and random–random pair counts, respectively. It is very important that the random sample has the same angular selection as the data pairs. For this purpose we constructed an angular mask using the software `mangle`[9] that describes the survey geometry in terms of disjoint spherical polygons. This mask accounts for the holes caused by bad-quality fields in SDSS, as well as the areas around bright stars selected from the *Tycho 2* catalog ($BTMAG < 11.5$). In addition, we also remove the areas around large ($>2''$) sources from the Two Micron All Sky Survey Extended Source Catalog that in some cases appear decomposed into multiple sources in *WISE*. Galactic absorption can have an impact in faint galaxy counts (Myers et al. 2006), so we mask out areas with $A_g > 0.18$. Finally, we avoid regions contaminated by the Moon and limit the sample to the rectangular area bounded by $135^\circ <$ R.A. $< 226^\circ$ and $1^\circ <$ decl. $< 54^\circ$ (J2000). These rather conservative limits avoid both the Galactic plane, where contamination by stars could present an issue, and the ecliptic pole, where the sensitivity of *WISE* improves substantially due to denser coverage and lower zodiacal background. Our selected area has a typical *WISE* coverage of ∼13 frames per bandpass.

[9] Available at http://space.mit.edu/~molly/mangle/.

### 4.2. Absolute Bias and Halo Masses of WISE AGNs

At small scales, the clustering of an extragalactic source population is difficult to predict due to processes such as merging and interactions. However, at larger scales (e.g., $>1$–$2\,h^{-1}$ Mpc), galaxy interactions have little impact and the galaxy correlation function follows that of the dark matter halos. At any redshift, massive halos cluster more strongly than less massive halos. Given an average redshift, this, in turn, allows one to estimate the typical mass of dark matter halos in which objects reside by estimating their absolute bias, i.e., their observed clustering level with respect to that of the underlying dark matter.

We compare our $w(\theta)$ measurements to the predictions of the standard cold dark matter (CDM) model in the linear perturbation theory of structure growth along with the nonlinear correction. To compute the dark matter angular two-point correlation function, $w_{\mathrm{dm}}(\theta)$, we use the nonlinear fitting function of Peacock & Dodds (1996) for the CDM power spectrum projected onto the same AGN redshift distribution. The bias factor is simply defined as $b \equiv (w(\theta)/w_{\mathrm{dm}}(\theta))^{1/2}$. In general, the bias is a function of scale, but under the assumption that galaxies cluster in a similar manner as dark matter, the bias factor is nearly scale-independent. This is particularly valid in the linear regime (i.e., large scales; see Verde et al. 2002). We limit the bias and the corresponding fits from $\theta = 0.^\circ04$ to $\theta = 0.^\circ4$, which corresponds to scales of roughly $\sim 800\,h^{-1}$ kpc to $\sim 8\,h^{-1}$ Mpc at $z \sim 1.2$.

Using an ellipsoidal collapse model, Sheth et al. (2001) related the halo bias factor to its mass and calibrated a fitting relation for a large library of cosmological $N$-body simulations:

$$b(M_{\mathrm{halo}}, z) = 1 + \frac{1}{\sqrt{a}\delta_c(z)}[\sqrt{a}(a\nu^2) + \sqrt{a}b(a\nu^2)^{1-c} - \frac{(a\nu^2)^c}{(a\nu^2)^c + b(1-c)(1-c/2)}], \quad (3)$$

where $a = 0.707$, $b = 0.5$, $c = 0.6$, and $\delta_c(z)$ is the critical density ratio for collapse given by Navarro et al. (1997) as $\delta_c(z) = 0.15(12\pi)^{2/3}\Omega_{mz}$, and $\Omega_{mz} \equiv (H_0/H(z))^2\Omega_m(1+z)^3$. $H(z)$ depends on the cosmology as $H^2(z) = H_0^2(\Omega_m(1+z)^3 + \Omega_\Lambda)$, and $\nu$ is defined as $\nu \equiv \delta_c z/\sigma(M)D(z)$, where $D(z)$ is the linear growth factor, here approximated analytically using the formulae by Carroll et al. (1992). The rms fluctuation of the density field is given by

$$\sigma^2(M_h) = \frac{1}{2\pi^2}\int_0^\infty k^2 P(k)\left[\frac{3(\sin(kr) - (kr)\cos(kr))}{(kr)^3}\right]dk, \quad (4)$$

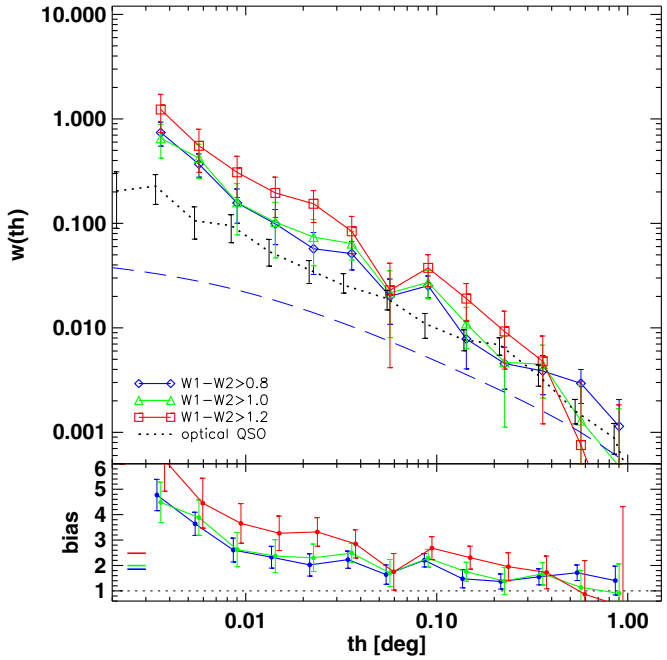


**Figure 10.** Angular correlation function $w(\theta)$ of *WISE*-selected AGNs with increasingly red $W1-W2$ color cuts. For reference, we also show data for optical quasars at $z_{\rm phot}<2.3$ from Myers et al. (2007, dotted line). Model predictions for the dark matter angular correlation function, $w_{\rm dm}(\theta)$ (dashed line), are computed using the Peacock & Dodds (1996) fitting function and the same AGN redshift distribution as the $W1-W2>0.8$ sample. The bottom panel shows the absolute bias $b=\sqrt{w/w_{\rm dm}}$. Markers on the left indicate the mean bias value over the range 0.°02–0.°4.

(A color version of this figure is available in the online journal.)

where the term in brackets represents the spherical top-hat window function (Peebles 1980) and the radius $r$ is related to the enclosed halo mass $M_h$ as

$$r=\sqrt[3]{\frac{3M_h}{4\pi\rho_0}}, \quad (5)$$

where $\rho_0$ is the present mean density of the universe, given by $2.78\times10^{11}\,\Omega_m\,h^2\,M_\odot\,{\rm Mpc}^{-3}$. The linear power spectrum of density fluctuations, $P(k)\propto T^2(q)\,k^n$ with $n=1$ (the Harrison–Zel'dovich case), is constructed using the fitting formula of Eisenstein & Hu (1998) for the transfer function $T(k)$ and normalized with the adopted value of $\sigma_8=0.84$ for $r=8\,h^{-1}$ Mpc.

## 5. RESULTS

### 5.1. Comparison to Optically Selected Quasars

We begin our analysis by exploring the angular clustering for the full sample of AGNs selected by *WISE*. Figure 10 shows that AGNs with $W1-W2>0.8$ present an angular correlation similar to that of optical quasars selected from SDSS by Myers et al. (2007) using a photometric kernel density estimation technique (Richards et al. 2004). A power-law fit of the form $w(\theta)=A\theta^{-\gamma}$ gives a value of $\gamma=1.03\pm0.11$ within the range $\theta=[0.°02–0.°5]$ ($\sim$0.4–10 $h^{-1}$ Mpc at $z=1.1$). Myers et al. (2006) find $\gamma=0.98\pm0.15$ for optically selected quasars at $z=1.4$, while Croom et al. (2005) find a slightly shallower value for 2QZ quasars, $\gamma=0.86\pm0.06$ when averaged over scales of 1–100 $h^{-1}$ Mpc and after correcting for redshift distortions. These slight differences are not entirely surprising considering the very different AGN selection criteria and the fact that the *WISE* AGN sample includes both obscured and unobscured AGNs, while the optical quasar samples are entirely composed of broad-lined, type-1 AGNs. Furthermore, the clustering of quasars might not be properly represented by a single power law.

At scales below $\theta\sim0.°1$, we find that redder AGNs have slightly higher angular clustering. This is interesting considering that this scale ($\sim2\,h^{-1}$ Mpc) marks the transition between the one-halo and two-halo terms, which, in the framework of halo clustering models, arises from galaxy pairs located in either the same or in two different halos, respectively. As shown at the bottom panel of Figure 10, the absolute bias for *WISE*-selected AGNs with $W1-W2>0.8$ with respect to the underlying dark matter distribution is $b=1.9\pm0.4$, as compared to $b=2.5\pm0.6$ for *WISE*-selected AGNs with redder mid-IR colors, $W1-W2>1.2$. Taking into account the caveat that different redshift and luminosity distributions can possibly bias the results, the simplest interpretation is that redder AGNs are hosted by slightly more massive dark matter halos. For type-1 AGNs at $z\lesssim2.5$ previous work has shown that the clustering depends only weakly on redshift, luminosity, or color (Shen et al. 2009; Ross et al. 2009). However, for type-2 AGNs this is mostly unknown and our $W1-W2>0.8$ sample is expected to be a mixture of both type-1 and type-2 AGNs. Finally, we note that our results compare well to the bias estimates obtained by Myers et al. (2007) for optical quasars over a similarly broad redshift range centered at $\langle z\rangle=1.4$.

### 5.2. Clustering of Red and Blue AGNs

We explore now the angular clustering of *WISE*-selected red and blue AGNs. The corresponding correlation functions, shown in Figure 11, display very different amplitudes. For a fixed slope $\gamma=1.03$ (that of the entire AGN sample), blue or unobscured AGNs (e.g., $r-W2\leqslant6$) have $A=0.0010\pm0.0002$, while red or obscured AGNs (e.g., $r-W2>6$) have $A=0.0039\pm0.0004$, i.e., a factor of $\sim$4 larger. The bottom panel shows that the mean bias of obscured sources relative to the dark matter is $b=2.9\pm0.6$, as compared to $b=1.6\pm0.6$ for unobscured AGNs. For reference, we also show in Figure 11 the angular clustering of type-1 quasars (gray shaded area) from Hickox et al. (2011), which is in broad agreement with our estimation for the blue AGN sample.

Part of the difference in clustering strength could, in principle, be due to the obscured sources having a different selection, that is, since obscured sources are required to be optically faint (or undetected), they could reside at slightly higher redshifts than their unobscured cousins. On the contrary, spectroscopy from both COSMOS and Boötes demonstrates that red AGNs tend to be at slightly lower redshift (Figure 7). The caveat is that there is a $\sim$20% incompleteness in the two spectroscopic samples and the sample sizes are not extremely large. While directly comparing the full and complete redshift distributions for blue and red *WISE*-selected AGNs would be ideal to check whether their different clustering strengths are related to different redshift distributions, we can nevertheless minimize it by selecting AGNs limited only to those with $r<23$ counterparts in SDSS. The amplitudes of the best-fit power law become $A=0.0024\pm0.0006$ for obscured AGNs, compared to $A=0.0012\pm0.0002$ for unobscured AGNs, for a fixed slope $\gamma=1.03$. Figure 12 shows the corresponding angular auto-correlations, illustrating once again that, while noisier, obscured AGNs have a correlation amplitude a factor of $\sim$2 larger than the unobscured sources.

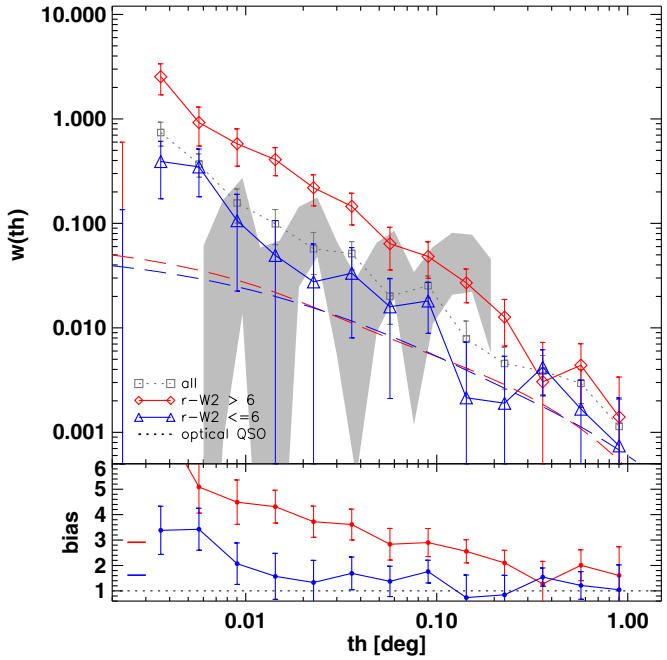


**Figure 11.** Angular correlation function $w(\theta)$ of *WISE*-selected AGNs split into obscured sources with $r-W2 > 6$ and unobscured AGNs with $r-W2 \leqslant 6$. The bottom panel shows the absolute bias with respect to the dark matter angular correlation (dashed line). Markers on the left indicate the mean bias value. The gray shaded region shows the angular autocorrelation of type-1 quasars from Hickox et al. (2011) (inferred from the quasar–galaxy and galaxy–galaxy correlation function), which is in broad agreement with our estimation for the blue AGN sample.

(A color version of this figure is available in the online journal.)

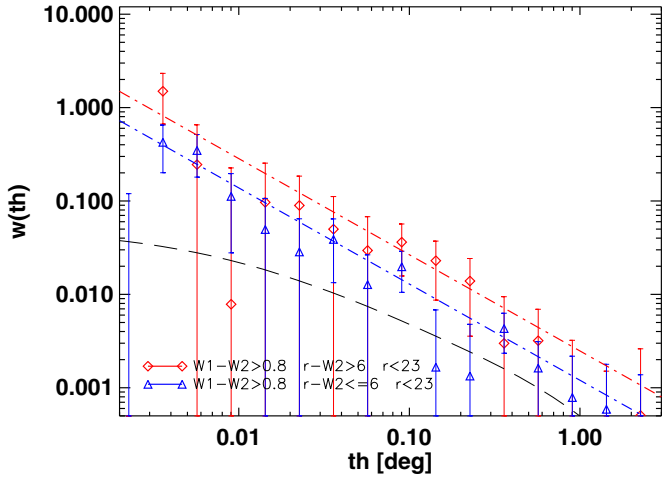


**Figure 12.** Angular correlation function $w(\theta)$ of *WISE*-selected AGNs as in Figure 11, but limited to sources with $r$-band counterparts brighter than $r = 23$ in SDSS. Simple power-law fits of the form $A\theta^{-\gamma}$ (dot-dashed lines) have a correlation amplitude a factor of ∼2 larger for the obscured population compared to the unobscured sources.

(A color version of this figure is available in the online journal.)

Given the difference in amplitude between the correlation functions of red and blue AGNs, we investigate how this reflects into the masses of dark matter halos that host them. Using the prescriptions described in Section 4.2, we estimate that blue AGNs at $z \sim 1$ are hosted in halos of characteristic mass $\log(M/M_{\odot}\,h^{-1}) = 12.37^{+0.57}_{-1.00}$. This is in excellent agreement with the halo mass of $\log(M/M_{\odot}\,h^{-1}) \sim 12.3$ reported by Ross et al. (2009) for SDSS optical quasars at $z < 2.2$. Croom et al. (2005) finds a similar value of $\log(M/M_{\odot}\,h^{-1}) \sim 12.5^{+0.2}_{-0.3}$ for 2QZ quasar hosts. In Figure 13 we show the bias as a function of redshift for the best-fit model (thick blue line), along with models of constant halo mass (dashed black lines) for reference. We find that the halos of our red AGNs have a much larger characteristic mass of $\log(M/M_{\odot}\,h^{-1}) = 13.48^{+0.54}_{-0.31}$, i.e., over a factor of 10 larger than for blue AGNs. We discuss the physical implications of this result in the following section. We also note that Hickox et al. (2011) reports a very similar mass of $\log(M/M_{\odot}\,h^{-1}) = 13.3^{+0.3}_{-0.4}$ for their obscured quasar sample, though their value of $\log(M/M_{\odot}\,h^{-1}) = 12.7^{+0.4}_{-0.6}$ for unobscured quasars is slightly larger than both our value and literature results for optically selected unobscured quasars.

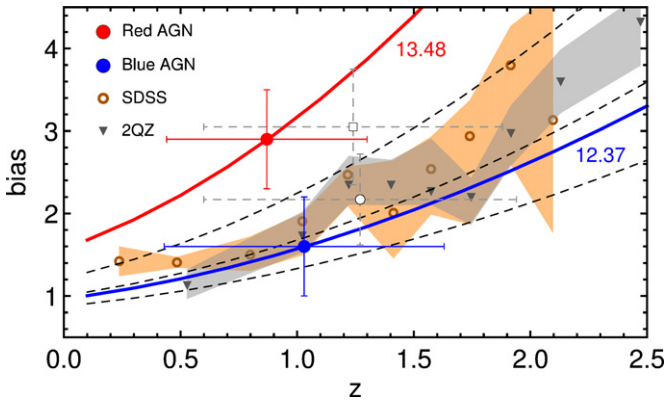


**Figure 13.** Bias as a function of redshift for *WISE* blue and red AGNs, shown at the mean redshift of their corresponding best-fit distributions. For reference, we also overlay data derived from optical SDSS quasars (orange, Ross et al. 2009) and 2QZ quasars (gray, Croom et al. 2005), as well as previous results from Hickox et al. (2011) for obscured (hollow square) and unobscured AGNs (hollow circle). Dashed lines are models of constant halo mass of $\log M/M_{\odot}\,h^{-1} = 13, 12.5, 12$ (from top to bottom), while the best-fit cases for *WISE* AGNs are indicated by solid, thick lines.

(A color version of this figure is available in the online journal.)

### 5.3. The Host Galaxies of WISE AGNs

To understand the clustering result of our red and blue samples, we study the host galaxies of *WISE*-selected AGNs using SED fitting and the morphology classifications discussed in Section 3.3. This is important because the observed difference in clustering might, in principle, be attributed to a selection effect that biases our red AGN sample to being hosted by early-type galaxies and our blue AGN sample to being hosted by late-type galaxies. Such a difference might be either the result of an intrinsic difference between the populations or due to a selection function bias. In particular, Figure 8 suggests that our red AGN sample could be biased against type-2 quasars in starburst galaxies if mid-IR-selected AGNs had a large spread over â values.

First, we use the SED fitting of *WISE*-selected AGN candidates in the Boötes field with the templates of Assef et al. (2010) to analyze the distribution of host light coming from each of the three galaxy templates (E, Sbc, and Im). From Figure 9, the blue AGN sample contains some sources with considerable dust obscuration (i.e., well above the $E(B-V) = 0.15$ boundary line). For these misclassified type-2 AGNs, we find that 38%, 36%, and 26% of their host galaxy emission is dominated by the E, Sbc, and Im templates, respectively, where we define an object to be dominated when >50% of the host luminosity is coming from a given template. These similar proportions suggest that

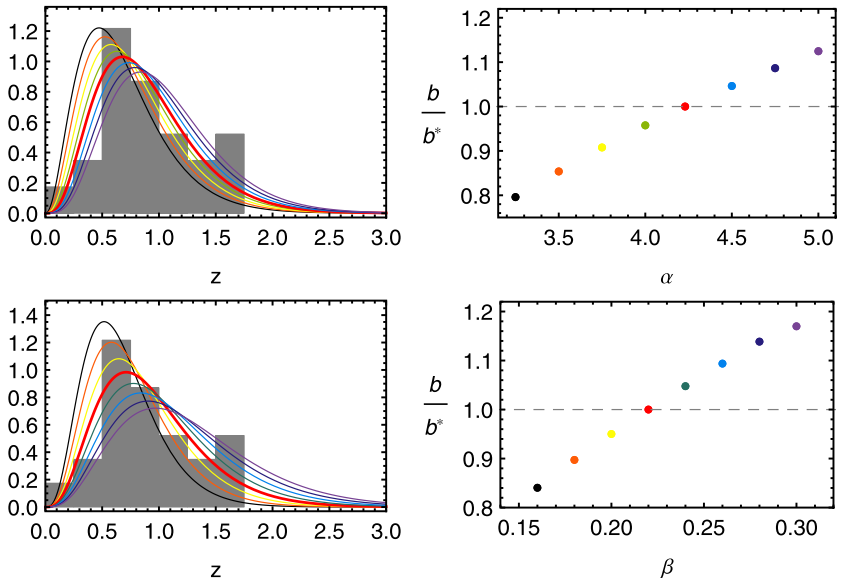


**Figure 14.** Top row: model redshift distributions of varying shape ($\alpha$) parameter along with the corresponding change in absolute bias normalized to the best-fitting case (red thick line) to COSMOS spectroscopic data for red AGNs (solid histogram). Bottom row: same as before but for distributions of varying scale ($\beta$) parameter. (A color version of this figure is available in the online journal.)

this selection bias, if present, is not preferentially missing Im galaxies, and therefore it is unlikely to be significantly affecting our results. For completeness, we note that it is difficult to determine the dominant host for the majority of blue candidates that have $E(B-V) < 0.15$, and thus AGN emission dominates the optical SED, making host SED fitting challenging.

The same analysis for red AGN candidates in Boötes gives 63%, 13%, and 24% of the cases dominated by E, Sbc, and Im templates, respectively. We note here that an E galaxy SED template does not directly imply that the galaxy morphology is elliptical. As discussed below, sources with the E-type template also include spiral galaxies with prominent bulges. Overall, there is also a large fraction of objects (37% if we combine Sbc and Im) dominated by late-type templates, suggesting that while early-type hosts are common, the red AGN population is hosted by a mixture of galaxy types.

Second, we recall the morphological results from Section 3.3. There we found that 54% (20%) of red (blue) AGNs have disks, while 32% (80%) are elliptical or point sources. This means that the red AGN sample is not dominated by typical red sequence galaxies, and that blue AGNs have, in fact, a lower fraction of late-type galaxies than red AGNs. These findings strongly suggest that it is unlikely that the clustering results are driven by host galaxy differences or selection bias. Instead, the observed differences in their correlation functions actually represent an intrinsic difference in the environments of type-1 and type-2 AGNs. Furthermore, as discussed in Section 6, the increase in clustering while moving from blue cloud to red sequence galaxies is markedly smaller than the difference between blue and red AGNs.

### 5.4. Sensitivity to Redshift Distribution

As the amplitude of $w(\theta)$ will certainly change depending on the location and shape of the redshift distribution in any observed sample of galaxies, it is important to assess how sensitive our bias estimates are to changes in the redshift distribution.

For this purpose we fit different model distributions for red and blue AGN redshifts and investigate how much the inferred absolute bias would change by systematically varying the distribution parameters with respect to the best-fitting case. To describe our redshifts, we adopt the Gamma statistical distribution of parameters $\alpha$ (shape) and $\beta$ (scale), although this choice is not critical (e.g., using Gaussians will lead to variations of the same order of magnitude). For red AGNs the best-fit parameters to observed COSMOS redshifts are $\alpha = 3.98$ and $\beta = 0.22$ ($\langle z \rangle = 0.88$), while for blue AGNs we obtain $\alpha = 2.65$ and $\beta = 0.39$ ($\langle z \rangle = 1.03$).

For our red AGN sample, in Figure 14 we reproduce the different model distributions with varying $\alpha$ (top row) and $\beta$ (bottom row), and the corresponding effect on the bias, always normalized to the best-fitting case highlighted in red. Changing $\alpha$ or $\beta$ within the range shown means that the bias could change by $\sim$20% at most. Note that to estimate $b/b^*$ we assume a spatial correlation length $r_0$ that is constant in redshift.

Figure 15 shows the same analysis applied to our blue AGN sample. The result is a similar variation of $\sim$25% in bias. In addition, we also test the effect of fitting a double Gamma distribution (dashed red line) instead of a single one. As expected, adding a second peak to the model naturally adjusts much better to the observed redshifts, yet the derived bias would decrease by only $\sim$6%. To further assess these conclusions, we repeated the test by directly convolving the COSMOS redshift distributions of blue and red AGNs with a Gaussian kernel of increasing width. Once again the bias changes by about 30% for any reasonable broadening. Note that adopting the Boötes redshift distributions as reference instead of COSMOS shifts these percentages by $\lesssim$4% and so does not qualitatively alter our conclusions. Finally, a bias uncertainty of $\sim$20% in the *least favorable* scenario—e.g., the blue AGN bias is underestimated by 20%, while the red AGN bias is overestimated by 20%—still translates into systematic halo mass estimates a factor of $\sim$3 larger for red AGNs than for blue AGNs.

## 6. DISCUSSION

In this work we have taken advantage of recently released data from *WISE* to construct a large sample of $\sim$170,000

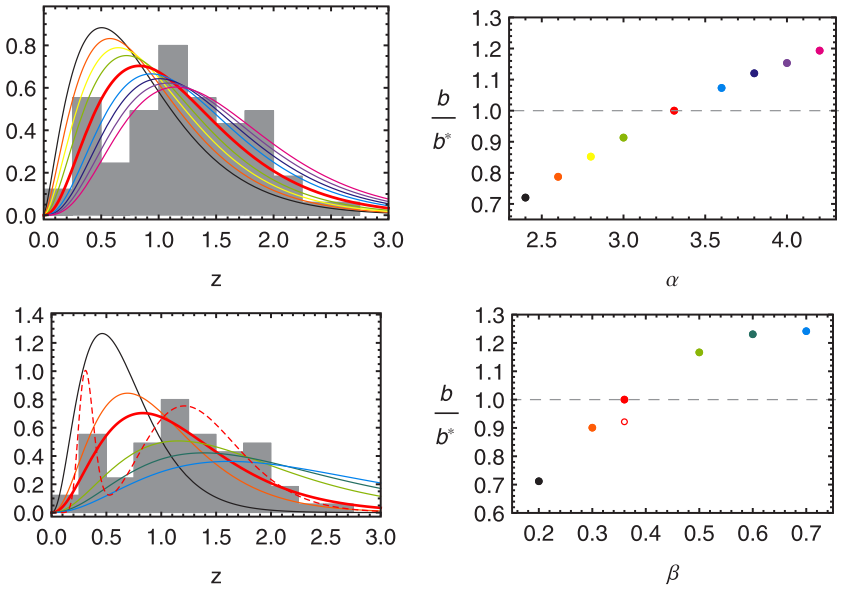


**Figure 15.** Same as Figure 14, but for the blue AGN sample. In addition, the bottom panels show the fit of a double Gamma distribution (dashed red line) along with the change in absolute bias (open circle) with respect to the single distribution case.
(A color version of this figure is available in the online journal.)

mid-IR-selected AGN candidates with the main purpose of analyzing their angular clustering properties. The selection is highly reliable (>90%), as demonstrated in Stern et al. (2012) and Assef et al. (2013), as well as by the high rate of X-ray detections (Section 3.1). The median redshift of the sample is $\langle z \rangle \sim 1.1$ based on relatively complete spectroscopy in the COSMOS and Boötes fields. By considering their optical counterparts from SDSS, we distinguish those *WISE*-selected AGNs that are optically faint, and thus have red optical-to-mid-IR colors and are inferred to be heavily obscured AGNs, from those that are optically bright, and thus have blue optical-to-mid-IR colors and are inferred to be unobscured AGNs.

We find that, as a whole, the *WISE*-selected AGN population presents a similar clustering strength to optically selected quasars at comparable redshifts, with a slightly higher absolute bias with respect to the dark matter distribution for redder $W1-W2$ subsamples. We find that the red AGNs show a notably larger bias level than that of blue AGNs, with $b = 2.9 \pm 0.6$ versus $b = 1.6 \pm 0.6$, respectively. Using a significantly smaller sample of few hundred sources over a much smaller area, Hickox et al. (2011) reported a similar absolute bias of $b = 2.87 \pm 0.77$ for obscured *Spitzer*-selected AGNs. Our absolute bias estimates suggest that red AGNs (i.e., obscured sources) are hosted by massive dark matter halos of $\log(M/M_{\odot}\,h^{-1}) \sim 13.5$, well above the halos of mass $\log(M/M_{\odot}\,h^{-1}) \sim 12.4$ that harbor blue AGNs (unobscured sources).

It is possible to interpret these results in a scenario where, at least during a brief phase before the dust is removed and the AGN gets "exposed," the black hole mass is a factor of a few below the $M - \sigma$ relation of active galaxies. For our sample, from the SED fits of *WISE* AGNs in Boötes we find that both red and blue AGNs have similar distributions of AGN bolometric luminosity, with a nearly identical mean of $\sim 2 \times 10^{12} L_{\odot}$. This suggests that the black hole masses of our red and blue AGNs do not differ much, and it is unlikely that their relative Eddington ratio is much different from unity. Moreover, their high luminosities are indicative of quasar-like accretion happening in both samples, and we know that *WISE* AGN selection tends to pick up AGNs radiating at large fractions of their Eddington limits (Assef et al. 2013). Since we find that obscured sources are hosted by more massive halos, then this means that, at least during a period of time, the black hole mass growth lags behind that of the hosting halos and hence the black holes in obscured AGNs are temporarily "undermassive" until they reach their final mass. This is not entirely surprising, as, for example, Alexander et al. (2008) find that submillimeter galaxies at $z = 2$ host black holes ~10 times smaller than expected for radio galaxies and quasars.

The basis of such a lag argument for AGNs has been proposed before in the literature (e.g., theoretically by King 2010, and coupled to clustering by Hickox et al. 2011). King (2010) suggests that the effect of Rayleigh–Taylor instabilities on the Eddington outflows that regulate black hole growth leads to black holes masses in active galaxies a factor of a few below the $M - \sigma$ relation, assuming that an observed AGN phase represents a black hole growth phase. Thus, AGNs should recurrently reach Eddington-order luminosities in order to grow fast enough to reach the masses specified by the Soltan (1982) relation.

One popular scenario for obscured quasars is that they represent an early evolutionary stage of rapid black hole growth just before the emergence of an unobscured, optical quasar. Hopkins et al. (2008) pose that in the final stages of coalescence of the galaxies, massive inflows supply large amounts of gas, increasing the gas density around nuclear regions and feeding the black hole that (1) initially is obscured, (2) grows accordingly at high Eddington rates, and (3) is small compared to the spheroid in formation. Then, any possible link between (final) black hole mass and halo mass (e.g., Ferrarese 2002) would predict dark matter halos of the same mass for obscured and unobscured sources. But, if obscured AGNs are an early stage where black holes are acquiring their final mass, then they would inhabit more massive halos when compared to unobscured quasars of the same black hole mass.

The clustering of red and blue galaxies has been studied in detail by Coil et al. (2008) using DEEP2 survey data.

They find that at $z \sim 1$ the bias of blue cloud galaxies is in the range of $b \sim 1.2$–$1.4$. Moving toward the red sequence, the bias increases by about 30%, so the measured bias of red galaxies is $b \sim 1.6$–$1.8$. Our blue AGN candidates have a bias that is at least comparable to luminous blue DEEP2 galaxies or to their less luminous red galaxies, but the bias of *WISE* red AGNs is much larger than that of red galaxies, and is well more than 30% greater than that of blue AGNs. This suggests that our red AGN candidates do not seem to cluster like typical red sequence galaxies at these redshifts and that the change in clustering is intrinsic to the two AGN types. These results are in broad agreement with Hickox et al. (2009), who finds that mid-IR-selected AGNs tend to reside in galaxies slightly bluer than the green valley, and with Griffith & Stern (2010), who conclude that the X-ray and mid-IR AGNs are not dominated by early-type galaxies, but by later-type galaxies with disks.

Finally, our results allow us to test a basic assumption of the AGN unification paradigm. A fundamental prediction of orientation-driven AGN unification models is that the angular clustering strength should be similar for obscured and unobscured AGNs. We find evidence that obscured AGNs are, in fact, more clustered than unobscured sources, which would appear to make simple orientation or obscuring torus scenarios much less plausible, or, at least, not the full story for AGN obscuration. Alternatively, it would be interesting to compare our results against predictions of more physical AGN models, where, for example, the sublimation radius changes with AGN power or the covering fraction depends on other physical parameters. Our data set does not allow us to test these models in detail, but larger samples with improved redshifts and spectral coverage will make it possible. Our primary result is a significant difference in the clustering of optically bright (blue) and optically faint (red) mid-IR-selected AGNs, implying that, on average, obscured and unobscured AGNs reside in different halos. This surprising result has important implications for AGN unification, the role of AGN feedback in galaxy formation, the lifetime of quasars, and understanding the sources responsible for the cosmic X-ray background and their cosmic evolution.

We thank A. Myers for useful replies to questions and extend our gratitude to the *WISE* extragalactic science team for its continuous support and interesting discussions over the years. We also gratefully acknowledge the anonymous referee and numerous colleagues, including G. Hasinger and R. Hickox, who provided insightful comments that have improved our discussion. This publication makes use of data products from the *Wide-field Infrared Survey Explorer*, which is a joint project of the University of California, Los Angeles, and the Jet Propulsion Laboratory/California Institute of Technology, funded by the National Aeronautics and Space Administration. Funding for the SDSS and SDSS-II has been provided by the Alfred P. Sloan Foundation, the Participating Institutions, the National Science Foundation, the U.S. Department of Energy, the National Aeronautics and Space Administration, the Japanese Monbukagakusho, the Max Planck Society, and the Higher Education Funding Council for England. The SDSS website is http://www.sdss.org/. R.J.A. was supported in part by an appointment to the NASA Postdoctoral Program at the Jet Propulsion Laboratory, administered by Oak Ridge Associated Universities through a contract with NASA. This research was partially supported by CONICET. R.J.A. was also supported in part by Gemini grant number 32120009. We also thank the NASA Astrophysics Data Analysis Program (ADAP) for its support.

## REFERENCES

Abazajian, K. N., Adelman-McCarthy, J. K., Agueros, M. A., et al. 2009, ApJS, 182, 543
Alexander, D. M., Brandt, W. N., Smail, I., et al. 2008, AJ, 135, 1968
Antonucci, R. R. J. 1993, ARA&A, 31, 473
Assef, R. J., Kochanek, C. S., Brodwin, M., et al. 2010, ApJ, 713, 970
Assef, R. J., Stern, D., Kochanek, C. S., et al. 2013, ApJ, 772, 26
Best, P. N., Kauffmann, G., Heckman, T. M., et al. 2005, MNRAS, 362, 25
Brusa, M., Civano, F., Comastri, A., et al. 2010, ApJ, 716, 348
Carroll, S. M., Press, W. H., & Turner, E. L. 1992, ARA&A, 30, 499
Coil, A. L., Newman, J. A., Croton, D., et al. 2008, ApJ, 672, 153
Coil, A. L., Georgakakis, A., Newman, J. A., et al. 2009, ApJ, 701, 1484
Croom, S. M., Smith, R. J., Boyle, B. J., et al. 2004, MNRAS, 349, 1397
Croom, S. M., Boyle, B. J., Shanks, T., et al. 2005, MNRAS, 356, 415
Cutri, R., et al. 2011, WISE Explanatory Supplement (IPAC, Pasadena), http://wise2.ipac.caltech.edu/docs/release/allsky/expsup/
Donley, J. L., Koekemoer, A. M., Brusa, M., et al. 2012, ApJ, 748, 143
Donoso, E., Li, C., Kauffmann, G., Best, P. N., & Heckman, T. M. 2010, MNRAS, 407, 107
Eisenstein, D. J., & Hu, W. 1998, ApJ, 496, 605
Elvis, M., Civano, F., Vignali, C., et al. 2009, ApJS, 184, 158
Falder, J. T., Stevens, J. A., Jarvis, M. J., et al. 2010, MNRAS, 405, 347
Ferrarese, L. 2002, ApJ, 578, 90
Georgakakis, A., Nandra, K., Laird, E. S., et al. 2007, ApJ, 660, 15
Gilli, R., Daddi, E., Zamorani, G., et al. 2005, A&A, 430, 811
Gilli, R., Zamorani, G., Miyaji, T., et al. 2009, A&A, 494, 33
Griffith, R. L., & Stern, D. 2010, AJ, 140, 533
Hasinger, G., Cappelluti, N., Brunner, H., et al. 2007, ApJS, 172, 29
Heisler, C. A., Lumsden, S. L., & Bailey, J. A. 1997, Natur, 385, 700
Hickox, R. C., Jones, C., Forman, W. R., et al. 2007, ApJ, 671, 1365
Hickox, R. C., Jones, C., Forman, W. R., et al. 2009, ApJ, 696, 891
Hickox, R. C., Myers, A. D., Brodwin, M., et al. 2011, AJ, 731, 117
Hopkins, P. F., Hernquist, L., Cox, T. J., & Kereš, D. 2008, ApJS, 175, 356
Jannuzi, B., Weiner, B., Block, M., et al. 2010, Bulletin of the American Astronomical Society Meeting 215, 42, 513
Jarrett, T. H., Cohen, M., Masci, F., et al. 2011, ApJ, 735, 112
King, A. R. 2010, MNRAS, 408, 95
Kirkpatrick, J. D., Cushing, M. C., Gelino, C. R., et al. 2011, ApJS, 197, 19
Kochanek, C. S., Eisenstein, D. J., Cool, R. J., et al. 2012, ApJS, 200, 8
Lacy, M., Storrie-Lombardi, L. J., Sajina, A., et al. 2004, ApJS, 154, 166
Landy, S. D., & Szalay, A. S. 1993, ApJ, 412, 64
Martínez-Sansigre, A., Karim, A., Schinnerer, E., et al. 2009, ApJ, 706, 184
Matthews, T. A., Morgan, W. W., & Schmidt, M. 1964, ApJ, 140, 35
Myers, A. D., Brunner, R. J., Richards, G. T., et al. 2006, ApJ, 638, 622
Myers, A. D., Brunner, R. J., Nichol, R. C., et al. 2007, ApJ, 658, 85
Navarro, J. F., Frenk, C. S., & White, S. D. M. 1997, ApJ, 490, 493
Peacock, J. A., & Dodds, S. J. 1996, MNRAS, 280, 19
Peebles, P. J. E. 1980, The Large-scale Structure of the Universe (Princeton: Princeton Univ. Press)
Richards, G. T., Vanden Berk, D. E., Reichard, T. A., et al. 2002, AJ, 124, 1
Richards, G. T., Nichol, R. C., Gray, A. G., et al. 2004, ApJS, 155, 257
Ross, N. P., Shen, Y., Strauss, M. A., et al. 2009, ApJ, 697, 1634
Schlegel, D. J., Finkbeiner, D. P., & Davis, M. 1998, AJ, 500, 525
Shen, Y., Strauss, M. A., Ross, N. P., et al. 2009, AJ, 697, 1656
Sheth, R. K., Mo, H. J., & Tormen, G. 2001, MNRAS, 323, 1
Soltan, A. 1982, MNRAS, 200, 115
Stern, D., Djorgovski, S. G., Perley, R., et al. 2000, AJ, 119, 1526
Stern, D., Eisenhardt, P., Gorjian, V., et al. 2005, ApJ, 631, 163
Stern, D., Assef, R. J., Benford, D., et al. 2012, ApJ, 753, 30
Stoughton, C., Lupton, R. H., Bernardi, M., et al. 2002, AJ, 123, 485
Tasse, C., Röttgering, H., & Best, P. N. 2011, A&A, 525, 127
Trump, J. R., Impey, C. D., McCarthy, P. J., et al. 2007, ApJS, 172, 383
Urry, C. M., & Padovani, P. 1995, PASP, 107, 803
Verde, L., Heavens, A. F., Percival, W. J., et al. 2002, MNRAS, 335, 432
Wright, E. L., Eisenhardt, P. R. M., Mainzer, A. K., et al. 2010, AJ, 140, 1868
Wylezalek, D., Galametz, A., Stern, D., et al. 2013, ApJ, 769, 79
Yan, L., Donoso, E., Tsai Chao-Wei,, et al. 2013, AJ, 145, 55
York, D. G., Adelman, J., Anderson, J. E., et al. 2000, AJ, 120, 1579